Characterization of the supermirror hard X-ray telescope for the InFOCμS balloon experiment

Takashi Okajima, Keisuke Tamura, Yasushi Ogasaka, Kazutoshi Haga, Seiji Takahashi, Satoshi Ichimaru, Hideo Kito, Shin'ichi Fukuda, Arifumi Goto, Kentaro Nomoto, Hiroyuki Satake, Seima Kato, Yuichi Kamata, Akihiro Furuzawa, Fumie Akimoto, Tsutomu Yoshioka, Kazumasa Kondo, Yoshito Haba, Takeshi Tanaka, Keiichi Wada, Noriyuki Hamada, Murat Hudaverdi, Yuzuru Tawara, Koujun Yamashita,

Department of Physics, Nagoya University, Nagoya 464-8602, Japan

okajima@u.phys.nagoya-u.ac.jp

Peter J. Serlemitsos, Yang Soong, Kai-Wing Chan, Scott M. Owens, Fred B. Berendse, Jack Tueller,

NASA Goddard Space Flight Center, Greenbelt, MD 20771, USA

Kazutami Misaki, Ryo Shibata, Hideyuki Mori, Kei Itoh,

Hideyo Kunieda, and

The Institute of Space and Astronautical Science, 3-1-1,

Yoshinodai, Sagamihara, Kanagawa 229-8510, Japan

Yoshiharu Namba

Department of Mechanical Engineering, Chubu University,

1200, Matsumoto-cho, Kasugai, Aichi 487, Japan

A hard X-ray telescope was successfully produced for balloon observations by making use of depth-graded multilayers, or so called *supermirrors*, with platinum-carbon (Pt/C) layer pairs. It consists of four quadrant units assembled in an optical configuration with a diameter of 40 cm and a focal length of 8 m. Each quadrant is made of 510 pieces of coaxially and confocally aligned supermirrors which significantly enhance the sensitivity in the energy range of 20 – 40 keV. The configuration of the telescope is similar to the X-ray telescope (XRT) on board *ASTRO-E*, but with the longer focal length. The reflectivity of supermirrors is on the order of 40 % in the energy range concerned at a grazing angle of 0.2 deg.. The effective area of a fully assembled telescope is 50 cm^2 at 30 keV. The angular resolution is 2.37 arcmin in half power diameter at 8.0 keV. The field of view is 12.6 arcmin in hard X-ray region somewhat depending on X-ray energies. These characteristics are discussed taking into account figure errors of reflectors and their optical alignment in the telescope assembly. This hard X-ray telescope is unanimously afforded to the InFOCμS balloon experiment.

OCIS codes: 110.6770, 230.4170, 340.7440, 340.7470, 340.7480

1. Introduction

X-ray telescope on board the *Einstein* and *ROSAT* satellites have successfully carried out X-ray imaging observations on a variety of astronomical objects in the soft X-ray region below a few keV.[1,2] The high-throughput X-ray telescopes on board the *ASCA* satellite[3] have made it possible to expand the high-energy limit to 10 keV by employing tightly nested thin-foil mirrors with grazing angles of 0.3 – 0.7 deg.. Subsequent further progress was made by the *Chandra* and *XMM-Newton* satellites.[4,5] However, they were not able to extend the high energy limit further by the use of grazing incidence X-ray configurations. The application of total external reflection for grazing incidence optics at higher energies becomes impractical, due to the very long focal lengths necessary to achieve large collecting area. Consequently observations in the hard X-ray region above 10 keV have been carried out by means of large area non-imaging detectors or a combination of coded masks and position-sensitive detectors. Their capability in angular resolution and background reduction are much behind focusing telescopes by orders of magnitude.

Hard X-ray observations are important to investigate objects strongly obscured by the absorption of neutral gas and non-thermal emissions from star-forming region, SNR, active galactic nuclei (AGN), clusters of galaxies, and so on. The imaging observations with high sensitivity have not yet been achieved in spite of those demands in astronomy.

The most promising development for hard X-ray telescopes is the use of Bragg reflection from periodic structures, complimenting total external reflection. Multilayers have the advantage of enhancing reflectivity in a narrow energy band beyond the critical energy. To broaden the sensitive energy band, multilayers stacked with graded periodic lengths (d), so

called *supermirrors*, are introduced.[6] At a fixed grazing angle, a gradual change of layer-pair thickness shifts the peak energy to be enhanced, while the reflectivity depends on the number of layer pairs. After intensive studies,[7] a design method called the "block method" is proposed, using multiple periodic Pt/C multilayers each with a different periodic thickness. This method has the great advantages of minimizing the number of layer pairs and yielding a flat response over a wide energy range. Yamashita *et al.*[8] demonstrated the performance of a hard X-ray focusing telescope using 10 sets of supermirrors designed by the block method.

InFOCμS (International Focusing Optics Collaboration for μCrab Sensitivity) is a collaboration between Nagoya University and NASA's Goddard Space Flight Center (GSFC), and will launch a series of balloon flights with multiple hard X-ray telescopes on board. The first of these flights took place in July, 2001 at the National Science Balloon Facility in Palestine, TX, with the first multilayer-based Wolter-I style X-ray telescope ever used for astronomical imaging, and a new solid-state Cadmium Zinc Telluride (CdZnTe) pixel detector[9] as the focal plane instrument. The aims of InFOCμS are to observe the celestial objects such as AGNs, SNRs, and clusters of galaxies in the hard X-ray band.

The first InFOCμS mirror consists of 2040 Pt/C supermirror foils. The supermirror foils produced at Nagoya University had the multilayer coating deposited on previously replicated Pt-coated aluminum foils, while those produced at GSFC were directly replicated multilayers. The foils were integrated into their quadrant housings at their respective institution, and the four quadrants were mated together at GSFC. In this paper, we present the X-ray characteristics of individual supermirrors and performance of the integrated quadrants that were produced at Nagoya University. We describe the design of the optical system in Section 2 and the fabrication and the reflectivity measurements of supermirrors in Section 3. We

present the characterization of the supermirror hard X-ray telescope in Section 4 and discuss their performance in comparison with the results of ray-tracing simulations in Section 5. Finally we summarize the characteristics of the telescope and the developments for future hard X-ray telescopes.

2. Design of the optical system

We have chosen the optical configuration of the hard X-ray telescope made of conical thin foil mirrors (170 μm thickness) which is similar to the *ASTRO-E* XRT. This configuration is suitable for the hard X-ray telescope which needs extremely small grazing incidence optics with a large aperture efficiency. However the *ASTRO-E* XRT has a focal length of 4.75 m corresponding to grazing angles from 0.18 to 0.6 deg. which limits the sensitive energy region to below 10 keV. The longer focal length of 8 meters will extend the energy range up to about 20 keV, while decreasing the grazing angles to 0.107 – 0.358 deg.. We have optimized the design parameters for a diameter of 40 cm and a focal length of 8 m. In this configuration, the number of nested mirror shells is 255 and the aperture efficiency is 55 %. In order to enhance the sensitivity beyond 20 keV, we need to introduce supermirrors.

The lower energy limit of X-rays is defined to be 20 keV by the absorption in the residual atmosphere at the balloon altitude of 40 km ($\sim$ 3 g/cm^2). The upper limit of the energy band is chosen to be 40 keV at the grazing angle of 0.36 deg., given by the minimum d of a multilayer of 2.5 nm. Therefore, the energy band for the InFOCμS balloon experiment is 20 – 40 keV. In this section we describe the design of the supermirrors and telescope under these conditions.

A. Design of supermirrors

The design of supermirrors used for a hard X-ray telescope has to satisfy many requirements, such as (1) high reflectivity in the 20 – 40 keV band with the grazing angle of 0.107 – 0.358 deg. to get a large effective area for the telescope, (2) flat and broad energy response, and (3) small number of layer pairs (N) to shorten the time of the mass production process. After intensive research of multilayers, we have selected a combination of platinum and carbon for this purpose.[13,14]

Figure 1 shows the calculated reflectivity of a Pt/C supermirror (thick solid curve) at a grazing angle of 0.183 deg., as designed by the block method.[8] Platinum and carbon are stacked as a top (vacuum side) and bottom (substrate side) layer within each layer, respectively. Thin curves show the reflectivity of each multilayer block stacked with different sets of d and N.

Broad peaks from left to right correspond to values of (d[nm], N) = (10.6, 1), (6.6, 2), (5.9, 4), (4.9, 8), (4.3, 11), and (3.8, 15) stacked in order from the reflecting surface toward the substrate. The total energy response of a supermirror is derived from a superposition of reflectivities of individual multilayer blocks. The peak reflectivity of deeper blocks has to be gradually increased to get flat response, because of attenuation by the upper blocks. For the energy range concerned, values of d and N for each block are thus determined, so that the reflectivity curve of each block is continuously connected to that of adjacent one without gaps or unnecessary overlaps. Another key parameter is a thickness ratio Γ of the heavy element d_H to d. The maximum reflectivity of the first order Bragg reflection is peaked for Γ around 0.5 and gradually decreases toward both sides. We have adopted $\Gamma = 0.4$ to make use

of the first order Bragg reflection for the deepest five multilayers, whereas $\Gamma = 0.63$ for the outermost bilayer (10.6, 1) to get high reflectivity by total external reflection. The Γ value of the top block was determined by trading off between enhancing the total external reflection and minimizing the attenuation for deeper multilayers. The most suitable thickness of Pt layer ($d \times \Gamma$) corresponds to the penetration depth ($Z_{1/e}$) at the critical energy (E_c) for a fixed grazing angle. This results in the smooth connection of reflectivity between the Bragg reflection and the total external reflection, as shown in Figure 1.

B. Design of the telescope

We have adopted the replication technique which was specially developed for the *ASTRO-E* XRT to transfer the smooth surface of a glass mandrel onto a thin aluminum foil substrate. The replication technique is described by Soong *et al.*[10] and Serlemitsos *et al.*.[11] The design uses two stage conical and coaxial mirror shells, which approximate the nested Wolter type I optics. Figure 2 shows the fabricated supermirrors and a quadrant of the InFOCμS telescope prepared by the Nagoya group. After the deposition of supermirrors on the thin foil substrates, they were assembled into a mirror housing.

As we mentioned above, the grazing angles of 255 pieces of nested mirror shells range from 0.107 to 0.358 deg.. These mirrors with different grazing angles are truncated into 13 different sets of supermirrors which are coated with identical design parameters within each set. The grazing angles in each group vary by less than 10 % of the mean value. As such, we can use the same block design for each foil in the group and still get a large effective area for the full telescope without any reductions due to shifts in the Bragg peak positions.

Special care was taken to make use of total external reflection at small grazing angles.

The critical angle (θ_c) and E_c is defined by the equation,

$$\theta_c[\mathrm{deg.}] \simeq 1.651 \times \left(\frac{\rho f_1}{A}\right)^{1/2} \frac{1}{E_c[\mathrm{keV}]}, \quad (1)$$

where ρ [g/cm^3] is the density of the surface material, f_1 is the atomic scattering factor, A is the atomic weight. So, for a grazing angle of 0.23 deg., the critical energy is $E_c = 20$ keV. In the design for the 1st to 10th group, a bilayer with the thickness of a platinum layer of $Z_{1/e}$ was additionally stacked on top of multilayers. Design parameters for all 13 groups are shown in Table 1. Figure 1 corresponds to the calculated reflectivities of the 6th group.

The effective areas of all 13 groups of mirror shells are shown in Figure 3. The thick curve indicates the sum of them, that is, the ideal total effective area of the full telescope. The energy range covered by each group is somewhat different, but the 20 – 40 keV band is fully covered by all groups. The contribution of each group to the total effective area is almost equal in the region of interest. A total effective area of more than 100 cm^2 in the 20 – 40 keV band is predicted.

Two quadrants were fabricated at Nagoya University and the other two at GSFC. The reflectors were produced in two ways; (1) supermirror deposition by the Nagoya team onto pre-replicated platinum foil substrates made by the GSFC team, and (2) direct replication of supermirrors deposited onto glass mandrels by the GSFC team. The direct replication of supermirrors is a newly developed technique by both groups.[15,16] This paper focuses on the fabrication and performance of the Nagoya quadrants. The characterization of the GSFC quadrants will be presented by Berendse *et al.*.[12]

3. Fabrication and characterization of supermirrors

A. Deposition of supermirrors

Two sets of DC magnetron sputtering systems are used for the deposition on the inner surfaces of cylindrical foil mirror substrates with radii of curvature of 60 – 200 mm and height of 100 mm. One system is specially designed to deposit multilayers onto the inner surfaces of conical mirror substrates.[14] It has two 10 cm diameter disk-type targets facing to each other, as shown in Figure 4. The argon plasma is confined in the cylindrical volume between them, so that mirrors are free from the damage caused by plasmas. A mask is mounted in front of the mirror substrate to control the flow of sputtered material and to keep the thickness of deposited layers uniform across the surface of the foils to within ± 2 %. The deposition rates of platinum and carbon are 0.16 nm/sec and 0.06 nm/sec on the surface of the substrate, respectively. The thickness is controlled by the rotation speed of the substrate around the sputtering target.

Another DC sputtering system has two large planar targets (75×250 mm), one for each material, which faces to the substrate (Figure 4). The non-uniformity along the vertical and azimuthal directions of the substrate is ± 2.5 % and ± 5 %, respectively. The deposition rates of platinum and carbon are 0.34 nm/sec and 0.12 nm/sec on the surface of substrate, respectively. The thickness of layers is controlled by the deposition time incorporated with shutter mechanism. The deposition for 1020 foils was completed within about 9 months.

B. Reflectivity measurements of supermirrors

We characterized each supermirror thus fabricated by measuring X-ray reflectivity as a function of grazing angles and energies with the X-ray beamline at Nagoya University. X-rays

are produced by a conventional rotating anode X-ray tube, with a tungsten anode, and a removable Ge(220) double crystal monochromator. X-rays are collimated to 0.1×1 mm^2 for horizontal and vertical directions, respectively. The W-Lα_1 line (8.4 keV) is used for monochromatic reflectivity vs. angle measurement. Continuum X-rays are used to measure the broad band reflectivity at fixed grazing angles. The reflected beam intensity and spectra are measured with a $3 \times 3 \times 2$ mm thick CdZnTe solid-state detector, which has a detection efficiency of almost 100 % in 10 – 100 keV range and an energy resolution of 3 % at 30 keV.

The surface of the foil mirror substrate is replicated from smooth glass mandrels with surface roughness less than 0.5 nm. Also the interfacial roughness of layer pairs significantly reduces the reflectivity from the ideal, depending on the relative thickness of each layer pair, d. The Debye-Waller (DW) factor is introduced to express the roughness (σ) through this paper. It is defined by the following equation;

$$R = R_0 \exp\left[-\left(\frac{2\pi m}{d}\sigma\right)^2\right], \tag{2}$$

where R is the measured reflectivity, R_0 is the ideal reflectivity, m is the order of Bragg reflection. The DW factor can be obtained by comparing the measured reflectivity at the Bragg peak with the ideal one.

Figure 5a through 5c show examples of measured reflectivity of supermirrors of group 3, 7, and 11 mentioned in Table 1. Those measurements are done with the continuum X-rays in a broad energy band. The reflectivity in the 20 – 40 keV region is shown to be more than 40 % at grazing angles less than 0.2 deg.. At grazing angles of about 0.3 deg., the reflectivities are reduced, but are still more than 20 %. While the broad band measurements are vital to proving the performance of our supermirrors, the critical parameters of a supermirror

are more clearly evaluated from the measurements of monochromatic reflectivity vs. angle. Figure 5d shows an example of the measured result of the 6th group with the angular scan using the W-Lα_1 line. The profile of the reflectivity fits well to the calculated one with $\sigma \simeq 0.4$ nm. A quarter of all supermirrors were evaluated by this method. Several samples of supermirrors were measured with monochromatized hard X-rays in 25 – 50 keV at a synchrotron radiation facility.[17] The roughness distribution is derived by the reflectivity measurements and shown in Figure 6. Average σ obtained during production was 0.38 ± 0.05 nm and 95 % of the measured data is within the range of 0.30 – 0.50 nm. This proves that our fabricated supermirrors are of sufficient quality for use in a hard X-ray telescope in 20 – 40 keV band.

After completion of segmented 1020 foil mirrors, we have assembled them in quadrants using the same techniques developed for the *ASTRO-E* XRT.[18]

4. Evaluation of the telescope

The performance of X-ray telescopes with supermirrors installed is evaluated in terms of (1) effective area, (2) field of view and (3) image quality (angular resolution). We performed each of these measurements on each of the Nagoya quadrants with the X-ray beamline at the Institute of Space and Astronautical Science (ISAS).

A. Measuring system

Continuum X-rays up to 50 keV are produced from the tungsten anode of the X-ray generator. The X-ray beam is collimated by a movable slit to 0.2×2.0 mm^2 in the horizontal and vertical directions, respectively, yielding a beam divergence of 1.2×12 arcseconds. An

NaI scintillation detector with a 25.4 mm diameter aperture and 17.3 % energy resolution at 22 keV is used to collect the focused radiation. We cannot use the CdZnTe detector used in the individual foil measurements, as it is smaller than the focused spot of a full quadrant. To illuminate the entire aperture of a quadrant uniformly with the narrow pencil beam, we perform raster scans of the X-ray beam by moving the telescope and detector synchronously. Note that the beam width of 2 mm in the vertical direction is effective to reduce the number of raster scans and hence speeds up the measuring process, while covering the entire geometric area of the quadrant. As noted above, the beam divergence in the vertical direction is 12 arcseconds, and does not contribute significantly to the measurement of effective area. Further details of the beamline system at ISAS, and the measuring methods for telescopes are described by Kunieda *et al.*[19] and Shibata *et al.*.[20]

Our measuring method is similar to the case of *ASTRO-E* XRT, except for the X-ray energies, the focal plane detector and its focal length. In the *ASTRO-E* case, the focal plane detector was placed at its focal length (4.5/4.75 m) away from the telescope. In this experiment, while the focal length of the mirror is 8 m, the focal plane detector was placed 4 m away from the mirror, due to the physical constraints of our vacuum chambers. To compensate, we move the detector at half the speed of the mirror during scans. Placing the detector at only half the the focal length does yield an image twice as large as that at the nominal focal plane, but this effect can be compensated for during data processing.

B. Measurement of Quadrants

1. Effective area

In Figure 7, open circles show the measured value of a quadrant multiplied by a factor of 4 to estimate the effective area of a full telescope. The dashed line and solid line show the calculated, ideal effective area with interfacial roughness of 0.0 nm and 0.38 nm. The latter value is the average value obtained by the reflectivity measurements mentioned in Section 3. The effective areas are estimated to be 66, 50 and 27 cm^2 at 20, 30 and 40 keV, respectively. Those values are smaller than the nominal by 34, 37 and 44 %, respectively. The reasons for those reductions are discussed in Section 5.

2. Field of view

We measured the angular response of the effective area (vignetting function) which is expressed as a function of off-axis angles. The vignetting function fits well to a Lorentzian curve and the FWHM is used to define the field of view. We measured the angular response in the sensitive ($\theta 1$) and insensitive ($\theta 2$) directions of each quadrant (See Figure 8c). Figure 8a and 8b show the vignetting function at 20, 30 and 40 keV for both directions. For the sensitive and insensitive directions, the field of view is 6.5 and 24.5 arcmin, respectively, and shows a weak dependence on X-ray energies. The angular response of the full telescope is the sum of responses for the two directions. The field of view of the full telescope is derived to be 12.6 arcmin in hard X-ray region.

3. Image quality

We also measured the intensity distribution with Cu-Kα_1 X-ray line (8.04 keV) in the on-axis direction of the telescope. An X-ray CCD camera (the window size of 25.4 × 25.4 mm) was used as the focal plane detector. The beam size was set to 0.5 × 0.5 mm^2, yielding a beam divergence is 3.4 arcsec. This is small enough to obtain an accurate half power diameter (HPD), without having to compensate for the beam divergence. The top panel of Figure 9 is a contour map of a quadrant on a logarithmic scale. The bottom panel shows the encircled energy function (EEF) which is the fraction of photons within a circle centered at the peak of the distribution. From this, we see that the angular resolution is 2.37 arcmin, HPD.

We also measured the effective area at 8.04 keV with NaI scintillation detector and a proportional counter. The effective areas are consistent with each other among those taken with three detectors. The effective area at 8.04 keV is estimated to be 333 cm^2 for the full telescope. This area is smaller than the ideal value by a factor of 29 %.

5. Discussion

A. Effective areas

As shown in Figure 7, the measured effective area is 71 % at 8.04 keV and 63 % at 30 keV relative to the nominal. The nominal values are derived from the product of the geometric area and the reflectivity of each supermirror with an average interfacial roughness of 0.38 nm. To investigate the reasons for this loss, we performed detailed reflectivity measurements of each pair of reflectors aligned in the optical configuration. The Cu-Kα_1 beam was collimated to 0.05 × 4.0 mm^2 in the horizontal and vertical directions, respectively. The beam size is much smaller than the projected width of each reflector, so we can measure the reflectivity in

the central part of each pair of foils. When the beam illuminates the edges of either foil, some photons are lost due to misalignment and slope errors. The beam spot is stepped in 0.05 mm increments along the radial direction of the quadrant, stopping for a 3 second exposure at each position. By comparing the total reflected intensity at each step with that of incident beam, we can map the local variation of the relative effective area.

Figure 10 shows the results of this measurement. The number of reflected photons expected from ideal shells is shown by the dashed line. Although the peak counts for each reflector is close to the ideal, the regions where each foil reflects well is somewhat narrower. As the radius and grazing angles become smaller, the peak counts significantly deviate from the expected values and the region of good reflection becomes much narrower. This result shows that photons are lost mostly at the edges of foils. We believe that due to figure errors, misalignment and shadowing by adjacent foils are the primary causes of the reduction seen above.

We found that the fractional loss of the effective area is 21 % in the local scanning measurement. This is still smaller than the reduction of 29 % reduction found in the raster scan of the full quadrant at 8.04 keV. This discrepancy is explained by large distortion at the azimuthal ends of each foil, where the fractional loss is found to be 40 %.

We performed a ray tracing simulation of the effective area taking into account figure errors of thin-foil mirrors and misalignment of assembled foils using scattering parameters derived during calibration of the *ASTRO-E* XRTs. Misalignment of foils is caused by the free play of foils in the support grooves. Foils with a 170 μm thickness can move in the alignment grooves by $\pm$ 13.2 μm, yielding a variation in on-axis incident angle of as much as 0.9 arcmin. On the other hand, figure errors in the reflecting surfaces can also cause fluctuation of the

local incident angles along each foil. This was evaluated by measuring the reflected X-ray beam profile as a function of scattering angle (θ_s). The scattering profile ($I(\theta_s)$) can be expressed by a combination of Gaussian, exponential and Lorentzian functions,

$$I(\theta_s) = N_{gau} \exp\left(-\frac{\theta_s^2}{2\sigma_{gau}^2}\right) + N_{exp} \exp\left(-\frac{|\theta_s|}{\sigma_{exp}}\right) + \frac{N_{lo}}{1 + \left(\frac{2\theta_s}{\sigma_{lo}}\right)^2}. \quad (3)$$

The best fit parameters are summarized in Table 2.

Taking into account these errors, the result of this ray tracing simulation is plotted with solid squares at 20, 30 and 40 keV in Figure 7. It turns out that the contributions of the figure error and misalignment to the reduction in effective area are 20 % and 11 % at 8 keV, and 22 % and 15 % at 30 keV, respectively. The simulated data points are consistent with the measured effective area at lower energies. Only the value at 40 keV is a little larger than the measured data. Since the energy response of supermirrors steeply drops at around 40 keV, this difference can be explained by the 5 % deviations in the layer-pair thickness of the supermirror coatings, as mentioned in Section 3.A.

The reduction factor of the effective area at 8.0 keV is 29 % compared with 20 % for *ASTRO-E* XRT. This is caused by the fact that our telescope has smaller grazing angles (0.1 – 0.35 deg.) than those of *ASTRO-E* XRT (0.18 – 0.6 deg.). At the smallest grazing angles (0.1 – 0.18 deg.), figure and alignment errors cause the largest reduction of 44 %, as indicated by the ray trace results and the local reflectivity measurements in Figure 10.

B. Image quality

In the conical approximation to the Wolter-I geometry, we approximate the hyperboloid and paraboloid surfaces by a conical shape. Due to this approximation, the image of a point-like X-ray source located at infinity has a minimum size of 22 arcsec, HPD. However, this does

not significantly contribute to the measured angular resolution of 2.37 arcmin, HPD.

The mirror substrates were fabricated with the replication method, and then supermirrors were deposited onto the surface. According to the calibration of *ASTRO-E* XRT, the measured angular resolution of a fully assembled mirror is typically about 2 arcmin, HPD, which is consistent with the results of quadrants of our hard X-ray telescope. This result means that the deposition of supermirrors doesn't significantly affect the image quality .

The measurement of the image quality of the InFOCμS quadrant was carried out with only soft X-rays (8.04 keV). In the previous experiment,[8] a PSF (point spread function) of the central core in the soft X-ray band was not different from that in hard energy bands, though the scattering tails were slightly higher for hard X-rays. The angular resolution in hard X-rays was larger than that in soft X-rays by about 20 %. Thus, the angular resolution of the InFOCμS mirror in the hard X-ray band is expected to be about 2.8 arcmin. The hard X-ray image quality will be confirmed by post-flight calibration.

6. Summary

The InFOCμS hard X-ray telescope is fully assembled with platinum-carbon multilayer supermirrors. These supermirrors are designed with the block method to obtain a flat response in the 20 – 40 keV band, while minimizing the number of layer pairs on each foil. The platinum thickness of the outermost layer is tuned to the penetration depth at the grazing angle and the critical energy where the supermirror is designed to maximize the contribution from total external reflection. X-ray measurements of a sample of production supermirrors confirm that the reflectivity is more than 40 % up to 40 keV at grazing angles of smaller than 0.2 deg., while the reflectivity is at least 20 % up to a grazing angle of 0.3 deg.. The

reduction rate of these measured reflectivity to ideal values can be attributed to the average interfacial roughness of 0.38 $\pm$ 0.05 nm.

We carried out effective area, field of view and image quality measurements of quadrants of the supermirror hard X-ray telescope at the ISAS 30 m beamline. The effective area is 66, 50 and 27 cm^2 at 20, 30 and 40 keV, respectively. The field of view is 12.6 arcmin in hard X-ray region and the angular resolution is 2.37 arcmin at Cu-Kα_1 (8.04 keV). The reduction of effective area of $30 - 44$ % from the designed value is explained by figure errors of reflector surfaces and misalignment of each reflector based on modeling of the *ASTRO-E* XRT.

Further improvements in effective area and image quality will be made by improving the foil figure and the accuracy of reflector alignment. We also plan to improve the interfacial roughness to better than 0.30 nm to provide higher reflectivity, as future hard X-ray missions are being designed for an energy band up to and beyond 100 keV.

Acknowledgments

This work was supported in part by a Grand in Aid of Specially Promoted Research contract No. 07102007 from the Ministry of Education, Culture, Sports, Science and Technology. T. Okajima acknowledges the Japan Society for the Promotion of Science for the support of his fellowship. The authors thank the team of engineers and technicians at GSFC for carrying out the actual work of the production of the foil substrates. The authors also thank the current and former students of Nagoya University who have been involved in the research and development of supermirror hard X-ray telescope.

References

1. R. Giacconi, G. Branduardi, U. Briel, A. Epstein, D. Fabricant, E. Feigelson, W. Forman, P. Gorenstein, J. Grindlay, H. Gursky, F. R. Harnden, Jr., J. P. Henry, C. Jones, E. Kellogg, D. Koch, S. Murray, E. Schreier, F. Seward, H. Tananbaum, K. Topka, L. Van Speybroeck, S. S. Holt, R. H. Becker, E. A. Boldt, P. J. Serlemitsos, G. Clark, C. Canizares, T. Markert, R. Novick, D. Helfand, and K. Long, "The Einstein (HEAO-2) X-ray Observatory," Astrophys. J. **230**, 540–550 (1979).

2. B. Aschenbach, "X-ray telescopes," Rep. Prog. Phys. **48**, 579–628 (1986).

3. P. J. Serlemitsos, L. Jalota, Y. Soong, H. Kunieda, Y. Tawara, Y. Tsusaka, H. Suzuki, Y. Sakima, T. Yamazaki, H. Yoshioka, A. Furuzawa, K. Yamashita, H. Awaki, M. Itoh, Y. Ogasaka, H. Honda, and Y. Uchibori, "The x-ray telescope onboard ASCA," Publ. Astron. Soc. Jpn. **47**, 105–114 (1995).

4. M. C. Weisskopf and S. L. O'dell, "Calibration of the AXAF observatory: overview," in *Grazing Incidence and Multilayer X-Ray Optical Systems*, R. B. Hoover and A. B. Walker, ed., Proc. SPIE **3113**, 2–17 (1997).

5. F. Jansen, D. Lumb, B. Altieri, J. Clavel, M. Ehle, C. Erd, C. Gabriel, M. Guainazzi, P. Gondoin, R. Much, R. Munoz, M. Santos, N. Schartel, D. Texier, and G. Vacanti, "XMM-Newton observatory. I. The spacecraft and operations," Astr. Astrophys. **365**, L1–L6 (2001).

6. K. D. Joensen, P. Hoghoj, F. E. Christensen, P. Gorenstein, J. Susini, E. Ziegler, A. K. Freund,

and J. L. Wood, "Multilayered supermirror structures for hard x-ray synchrotron and astrophysics instrumentation," in *Multilayer and Grazing Incidence X-Ray/EUV Optics II*, R. B. Hoover and A. B. Walker, eds., Proc. SPIE **2011**, 360–372 (1994).

7. K. Yamashita, K. Akiyama, K. Haga, H. Kunieda, G. S. Lodha, N. Nakajo, N. Nakamura, T. Okajima, K. Tamura, and Y. Tawara, "Fabrication and characterization of multilayer supermirrors for hard X-ray optics," J. Synchrotron Rad. **5**, 711–713 (1998a).

8. K. Yamashita, P. J. Serlemitsos, J. Tueller, S. D. Barthelmy, L. M. Bartlett, K.-W. Chan, A. Furuzawa, N. Gehrels, K. Haga, H. Kunieda, P. Kurczynski, G. Lodha, N. Nakajo, N. Nakamura, Y. Namba, Y. Ogasaka, T. Okajima, D. Palmer, A. Parsons, Y. Soong, C. M. Stahl, H. Takata, K. Tamura, Y. Tawara, and B. J. Teegarden, "Supermirror hard-x-ray telescope," Appl. Opt. **37**, 8067–8073 (1998b).

9. W. H. Baumgartner, J. Tueller, S. Barthelmy, H. Krimm, F. Birsa, and L. Ryan, "The CZT Pixellated Detectors on the InFOCμS Hard X-ray Telescope," in *New Century of X-ray Astronomy*, H. Kunieda and H. Inoue eds., A. S. P. Conference Series **251**, 520–521 (2001).

10. Y. Soong, L. Jalota, P. J. Serlemitsos, "Conical thin foil x-ray mirror fabrication via surface replication", in *X-Ray and Extreme Ultraviolet Optics*, R. B. Hoover and A. B. Walker, eds, Proc. SPIE **2515**, 64–69 (1995).

11. P. J. Serlemitsos and Y. Soong, "Foil x-ray mirrors," Astrophys. Space Sci. **239**, 177–196 (1996).

12. F. Berendse, S. M. Owens, P. J. Serlemitsos, J. Tueller, K.-W. Chan, Y. Soong, H. Krimm, W.

H. Baumgartner, Y. Ogasaka, K. Tamura, T. Okajima, Y. Tawara, K. Yamashita, K. Misaki, and H. Kunieda are preparing a manuscript to be called "Production and performance of the InFOCμS 20–40 keV graded multilayer mirror."

13. Y. Tawara, K. Yamashita, H. Kunieda, K. Haga, K. Akiyama, A. Furuzawa, Y. Terashima, and P. J. Serlemitsos, "Multilayer supermirror coating for hard-x-ray telescope," in *Multilayer and Grazing Incidence X-Ray/EUV Optics III*, R. B. Hoover and A. B. Walker, eds., Proc. SPIE **2805**, 236–243 (1996).

14. K. Tamura, K. Yamashita, H. Kunieda, Y. Tawara, A. Furuzawa, K. Haga, G. Lodha, N. Nakajo, N. Nakamura, T. Okajima, O. Tsuda, P. J. Serlemitsos, J. Tueller, R. Petre, Y. Ogasaka, Y. Soong, and K.-W. Chan, "Development of balloon-borne hard-x-ray telescopes using a multilayer supermirror," in *Grazing Incidence and Multilayer X-Ray Optical Systems*, R. Hoover and A. B. Walker, eds., Proc. SPIE **3113**, 285–292 (1997).

15. A. Furuzawa, K. Yamashita, H. Kunieda, Y. Tawara, K. Tamura, K. Haga, N. Nakamura, N. Nakajo, H. Takata, T. Okajima, Y. Ogasaka, G. S. Lodha, and Y. Namba, "Replication of a multilayer supermirror," in *X-Ray Optics, Instruments, and Missions*, R. B. Hoover and A. B. Walker, eds., Proc. SPIE **3444**, 569–575 (1998).

16. S. M. Owens, T. Okajima, Y. Ogasaka, F. Berendse, and P. J. Serlemitsos, "Multilayer coated thin foil mirrors for InFOCμS" in *X-Ray Optics, Instruments, and Missions III*, J. E. Truemper and B. Aschenbach, eds., Proc. SPIE **4012**, 619–625 (2000).

17. T. Okajima, S. Ichimaru, K. Tamura, K. Haga, Y. Ogasaka, S. Takahashi, S. Fukuda, H.

Kitou, A. Gotou, Y. Tawara, K. Yamashita, Y. Tsusaka, S. Takeda, and H. Kunida, "The X-ray measurement of the supermirror using synchrotron radiation," in *Advances in X-Ray Optics*, A. K. Freund, T. Ishikawa, A. M. Khounsary, D. C. Mancini, A. G. Michette, and S. Oestreich, eds., Proc. SPIE **4145**, 53–60 (2000).

18. H. Kunieda, M. Ishida, T. Endo, Y. Hidaka, H. Honda, K. Imamura, J. Ishida, M. Maeda, K. Misaki, R. Shibata, A. Furuzawa, K. Haga, Y. Ogasaka, T. Okajima, Y. Tawara, Y. Terashima, M. Watanabe, K. Yamashita, T. Yoshioka, P. J. Serlemitsos, Y. Soong, and K.-W. Chan, "X-ray telescope onboard Astro-E: optical design and fabrication of thin foil mirrors," Appl. Opt. **40**, 553–564 (2001).

19. H. Kunieda, Y. Tsusaka, H. Suzuki, Y. Ogasaka, H. Awaki, Y. Tawara, K. Yamashita, T. Yamazaki, M. Itoh, T. Kii, F. Makino, Y. Ogawara, H. Tsunemi, K. Hayashida, S. Nomoto, M. Wada, E. Miyata, and I. Hatsukade, "Thirty-meter x-ray pencil beam line at the Institute of Space and Astronautical Science," Jpn. J. Appl. Phys. **32**, 4805–4813 (1993).

20. R. Shibata, M. Ishida, H. Kunieda, T. Endo, H. Honda, K. Misaki, J. Ishida, K. Imamura, Y. Hidaka, M. Maeda, Y. Tawara, Y. Ogasaka, A. Furuzawa, M. Watanabe, Y. Terashima, T. Yoshioka, T. Okajima, K. Yamashita, P. J. Serlemitsos, Y. Soong, and K.-W. Chan, "X-ray telescope onboard Astro-E. II. Ground-based x-ray characterization," Appl. Opt. **40**, 3762–3783 (2001).

21. K. Misaki, H. Kunieda, M, Ishida, T. Endo, Y. Hidaka, H. Honda, K. Imamura, J. Ishida, M. Maeda, R. Shibata, H. Mori, K. Itoh, A. Furuzawa, K. Haga, Y. Ogasaka, T. Okajima, Y.

Tawara, Y. Terashima, M. Watanabe, K. Yamashita, T. Yoshioka, P. J. Serlemitsos, Y. Soong, and K.-W. Chan are preparing a manuscript to be called "X-ray telescope onboard Astro-E. III. guideline to performance improvements and optimization of ray-tracing program."

Fig. 1. Calculated reflectivity of the 6th group of supermirrors (thick solid line) at a grazing angle of 0.183 deg.. Six multilayers (thin lines) are stacked successively and on top of them a thick platinum layer is deposited to provide total external reflection up to 55 keV. The parameters of each block are presented in Table 1 as the 6th group supermirror.

Fig. 2. Fabricated supermirrors 2a and a quadrant 2b of the InFOCμS telescope prepared by Nagoya group. The total number of supermirrors is 1020 for two quadrants. Radii of thin foil mirrors range from 60 mm to 200 mm and their height and thickness are 100 mm and 170 μm, respectively. Supermirrors are assembled into a housing, following the Wolter type I configuration. The height of the housing is 230 mm, and the outer radius is 220 mm. Assembled supermirrors are seen on the top of the housing.

List of Figures

Fig. 3. Effective areas of each mirror group (thin lines) and of a full telescope (thick solid line). Among the 13 groups, the inner 10 groups have an outermost platinum layer as thick as the 1/e penetration depth of X-rays at the designated energy for each foil, and their effective areas have a smooth continuation to lower energy. The outer three groups have a dip at 15 keV, since total external reflection by a single platinum layer is no longer effective. All groups show almost the same effective area in 20 – 40 keV band.

Fig. 4. Schematic view of the DC magnetron sputtering system. The Left figure shows the sputtering system which has two disk-type sputtering targets facing each other. An argon plasma is created between the two targets, and substrates rotate around the sputter sources during deposition. The right figure shows another sputtering system which has a linear sputter target facing a fixed substrate.

Fig. 5. Measured reflectivity of supermirrors (dots with error bars) deposited on pre-replicated foil substrates. Figures 5a – 5c show the reflectivity vs. energy at grazing angles of 0.138, 0.190 and 0.295 deg., respectively. Overlaid dashed lines show the best fitted reflectivity curve with parameters of 3rd, 7th and 11th group in Table 1 and interfacial roughness of 0.35, 0.40 and 0.43 nm (DW), respectively. The calculation includes the CdZnTe detector response, which has an energy resolution of 3 % at 30 keV. Figure 5d shows the reflectivity of a 6th group supermirror measured at 8.4 keV (W-Lα_1). The overlaid curve is calculated with an interfacial roughness of 0.45 nm (DW). The parameters are summarized in Table 1.

Fig. 6. Histogram of the distribution of the interfacial roughness of fabricated supermirrors derived from the measurements of the reflectivity of 250 production supermirrors. The average value of the interfacial roughness is 0.38 ± 0.05 nm.

Fig. 7. On-axis effective area of the full X-ray telescope. Open circles show the measured effective area of one quadrant multiplied by a factor of 4. The dashed and solid curves show the calculated values with interfacial roughnesses of 0 nm and 0.38 nm, respectively. The measured effective area is lower than the calculation by about 40 %. Squares show the results of ray-tracing simulation with the interfacial roughness of 0.38 nm. This model calculation method was developed for the *ASTRO-E* XRT calibration including alignment and surface figure errors.

Fig. 8. Vignetting functions of a quadrant measured with hard X-rays. The squares, triangles, and circles present the data at 20, 30, and 40 keV, respectively. Figures 8a and 8b show the sensitive ($\theta 1$) and insensitive ($\theta 2$) directions, respectively. Solid lines are Lorentzian functions fitted to the measured data. The FWHM of each function for the sensitive direction is 7.7, 6.5, and 5.2 arcmin for 20, 30, and 40 keV, respectively. For the insensitive direction, the FWHM is 25.8, 24.4, and 23.2 arcmin for 20, 30, and 40 keV, respectively. Figure 8c shows a schematic view of the configuration for off-axis measurements.

Fig. 9. On-axis look-down image (top) and Encircled Energy Function (EEF, bottom) of a quadrant, measured at Cu-Kα_1 (8.04 keV) with a beam size of 0.5×0.5 mm^2. The contours in the left plot are drawn on logarithmic scale. The large distortion of the image is primarily caused by the edge shape of mirror shells. The EEF is derived by counting the number of photons within a circle of arbitrary radius, compared to the total number of photons in a 10 arcmin radius.

Fig. 10. Results of local reflectivity measurements. Abscissa; radial position of the beam. Ordinate; number of reflected photons with 3-sec-exposure at every stop. Data for inner, middle and outer reflectors are shown in panels from the top to the bottom. Dots with error bars are the data points, and dashed lines are the expected number of photons for ideal foil. The loss of effective areas is 46, 23 and 15 % from the top figure to the bottom, respectively.

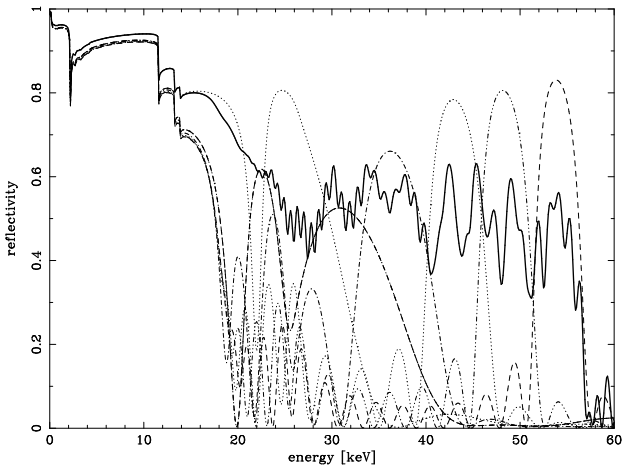

Figure 1, T. Okajima et. al.

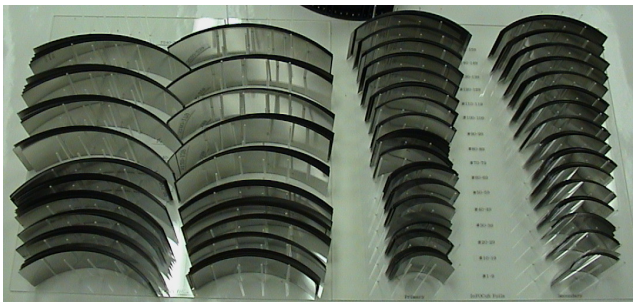

Figure 2a, T. Okajima et. al.

Figure 2b, T. Okajima et. al.

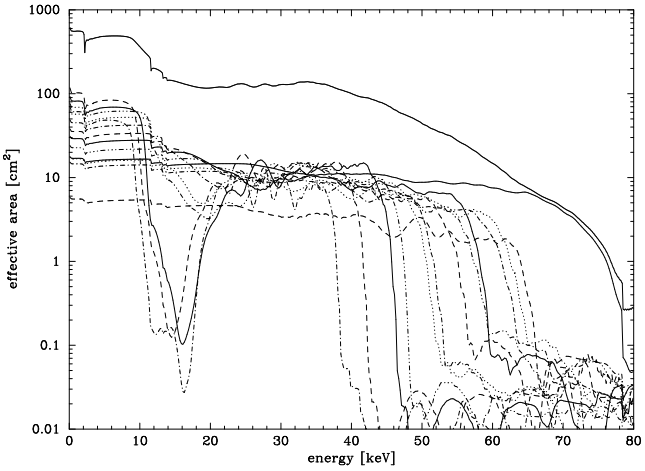

Figure 3, T. Okajima et. al.

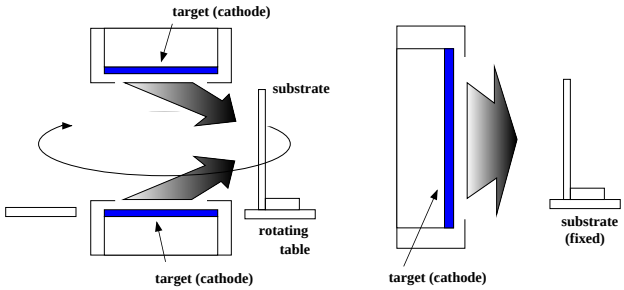

Figure 4, T. Okajima et. al.

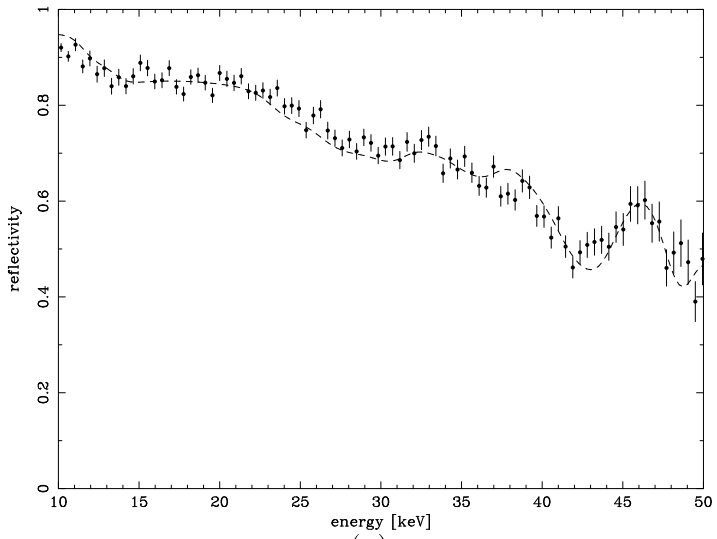

(a)

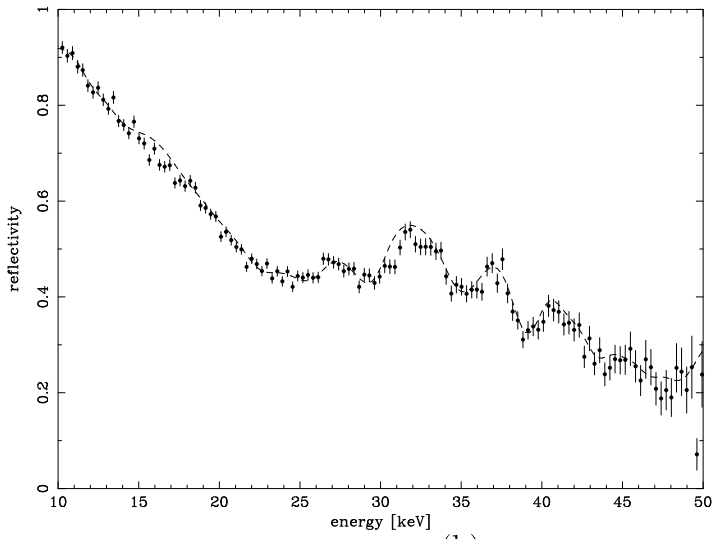

(b)

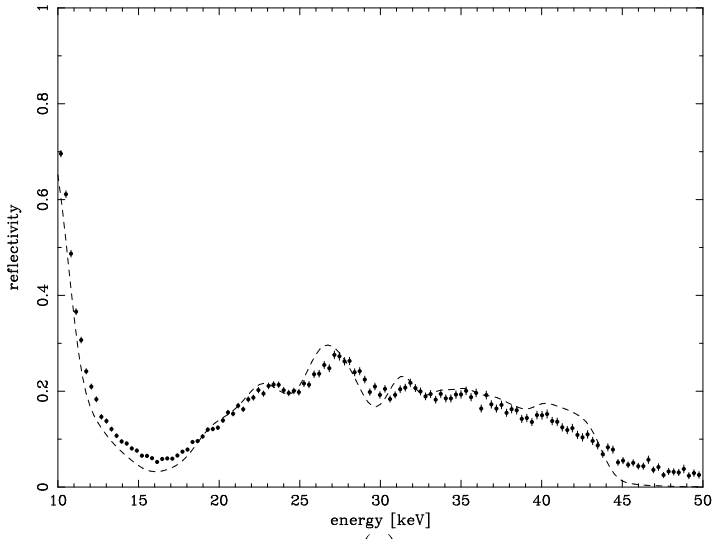

(c)

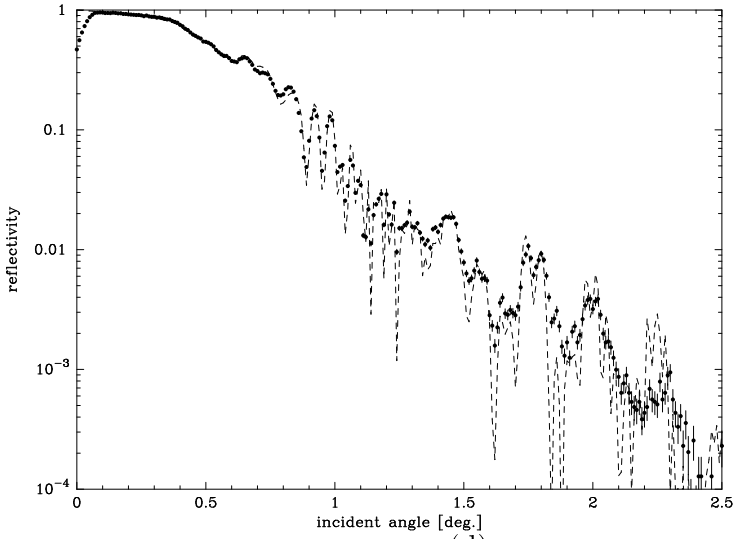

(d)

Figure 5, T. Okajima et. al.

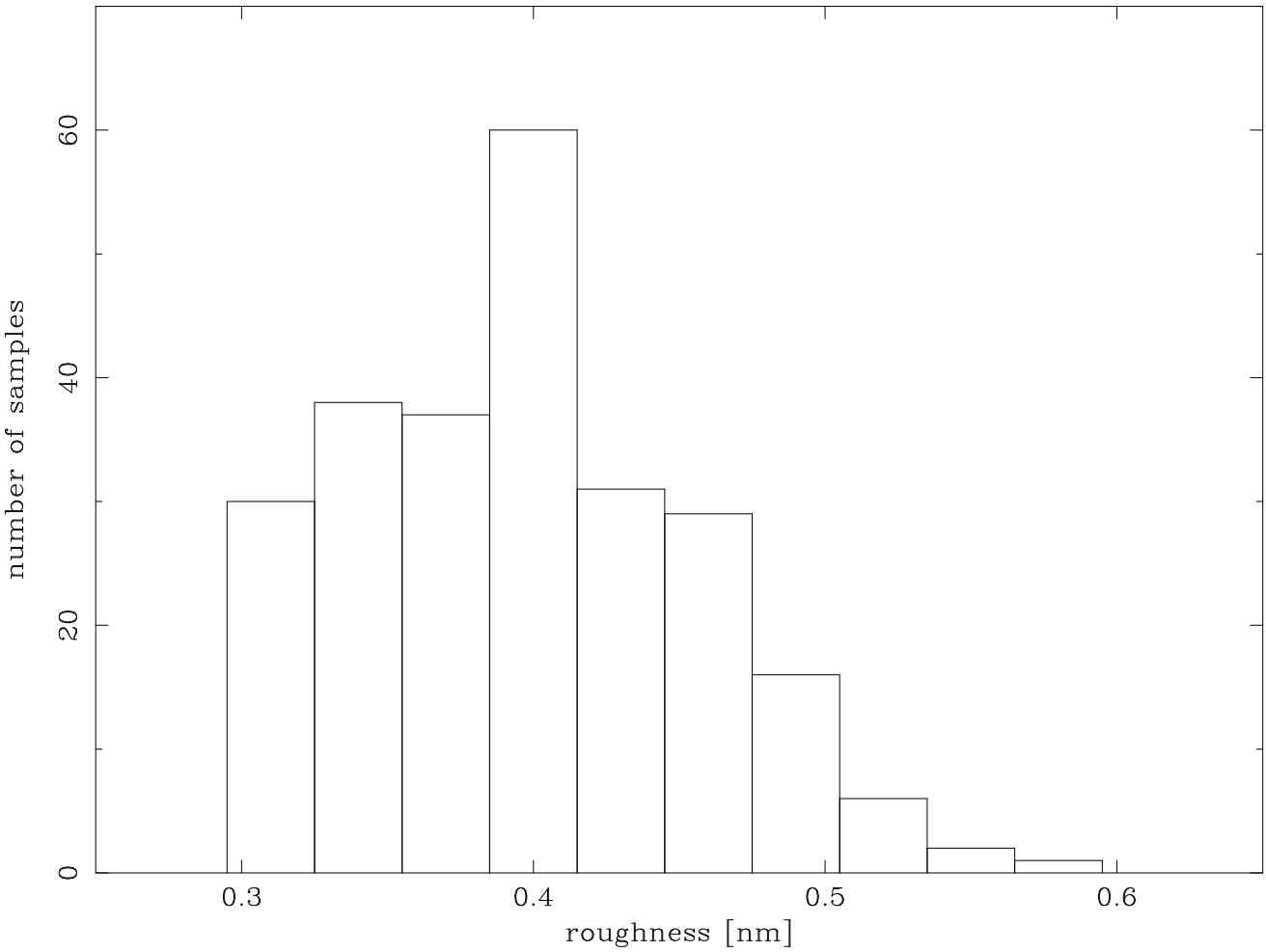

Figure 6, T. Okajima et. al.

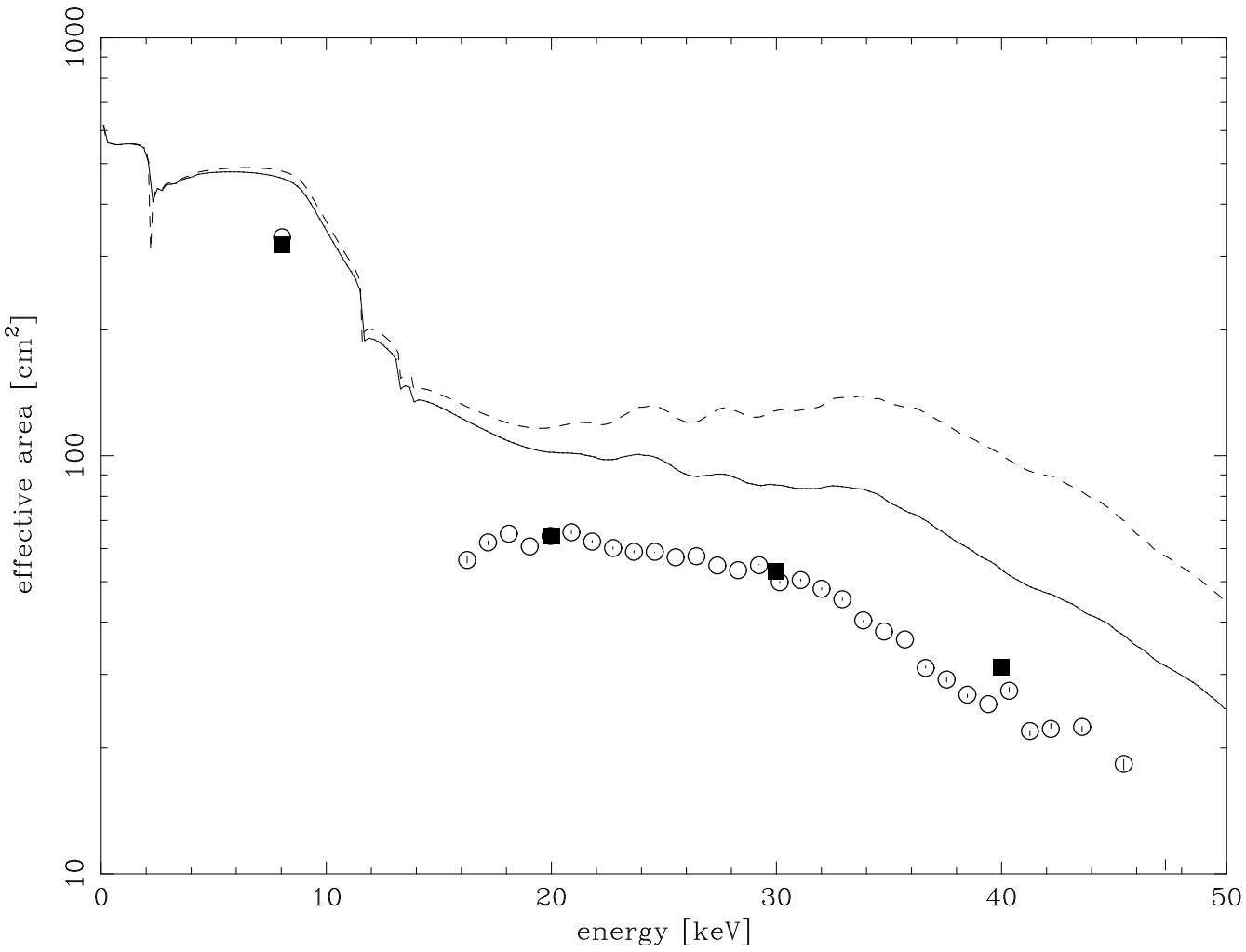

Figure 7, T. Okajima et. al.

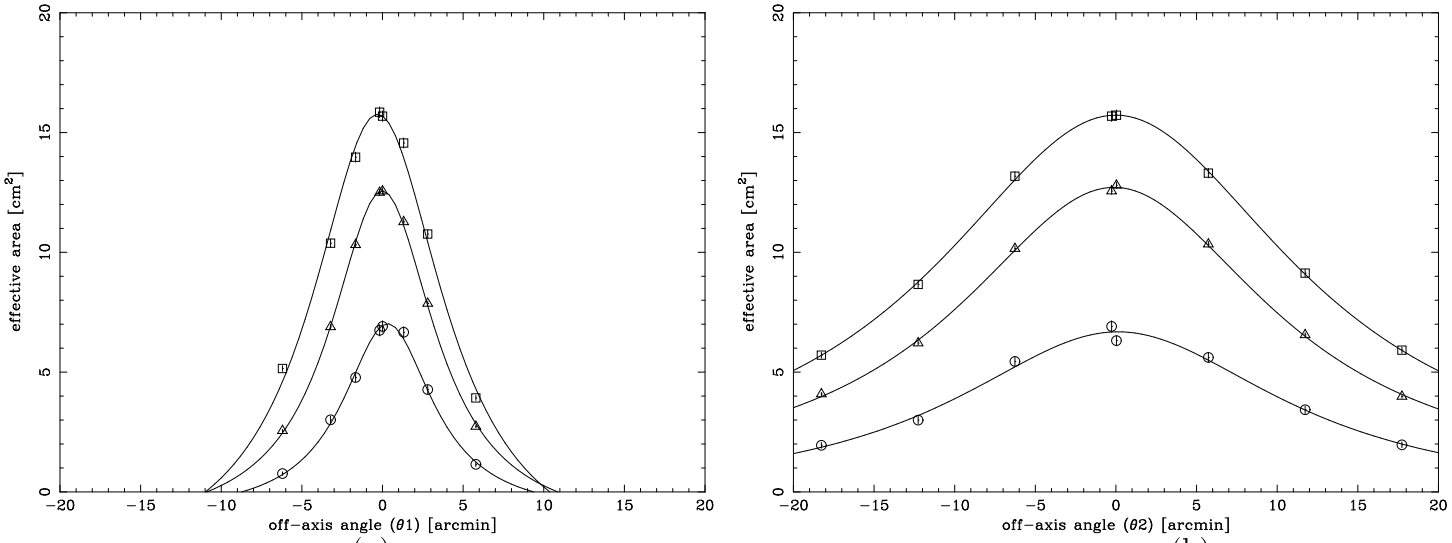

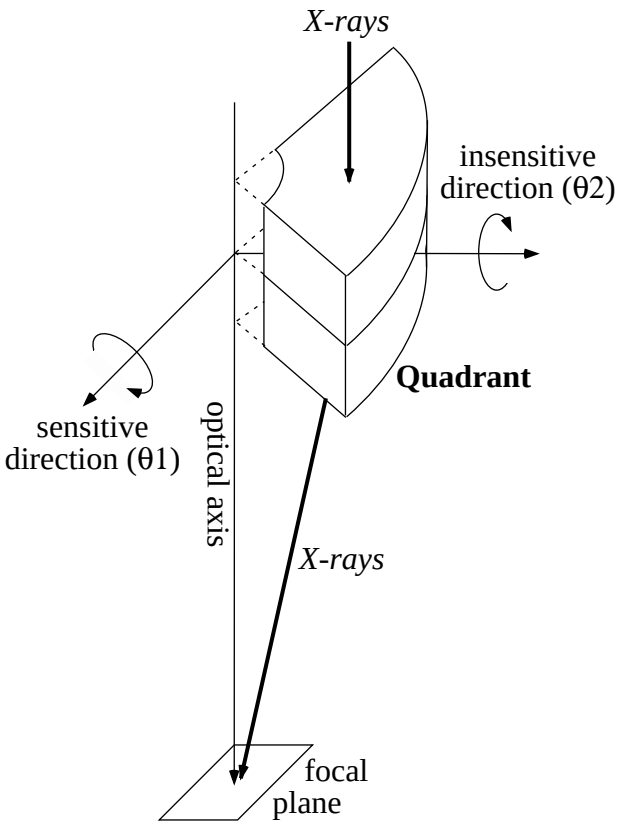

(c)

Figure 8, T. Okajima et. al.

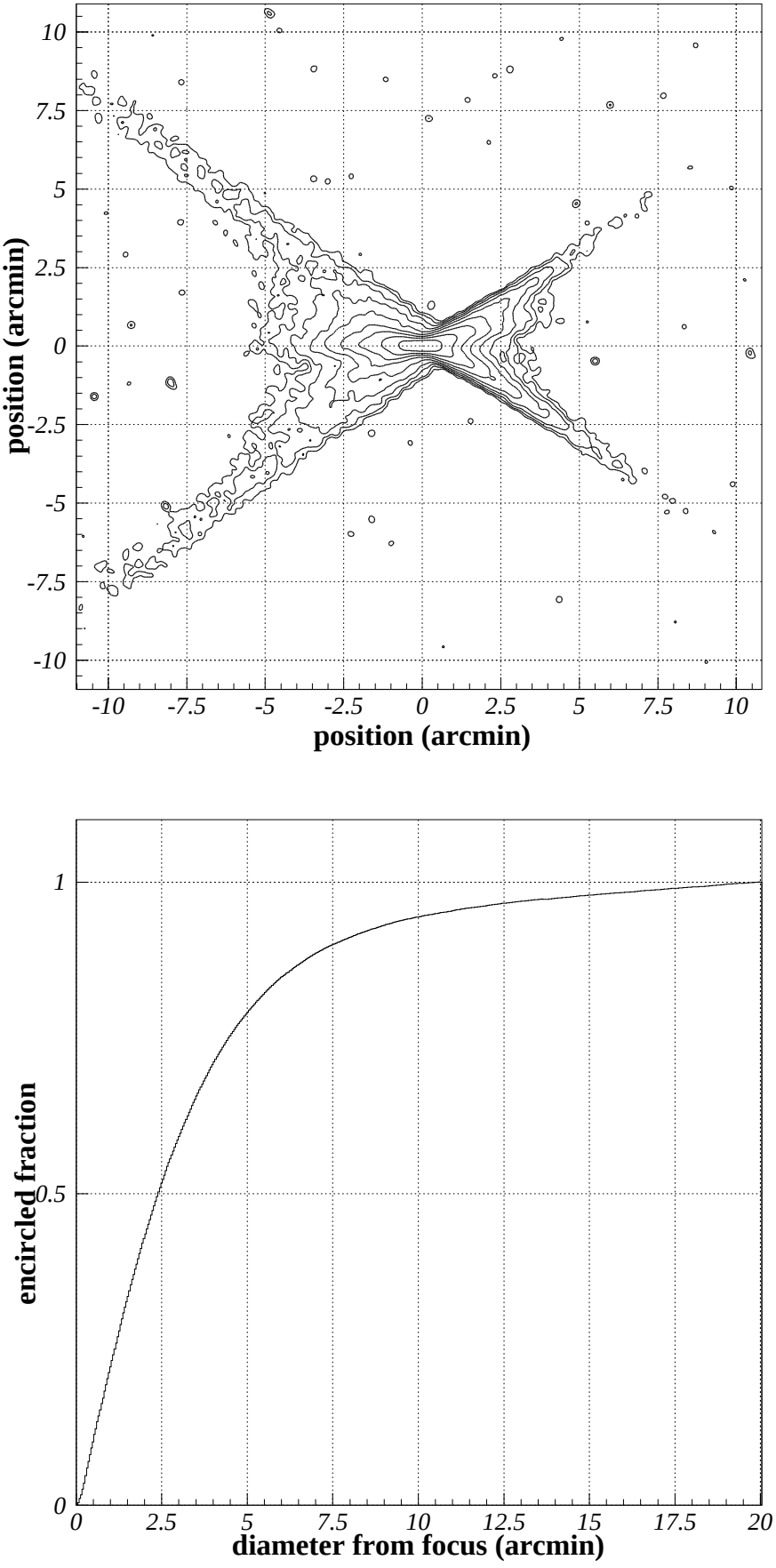

Figure 9, T. Okajima et. al.

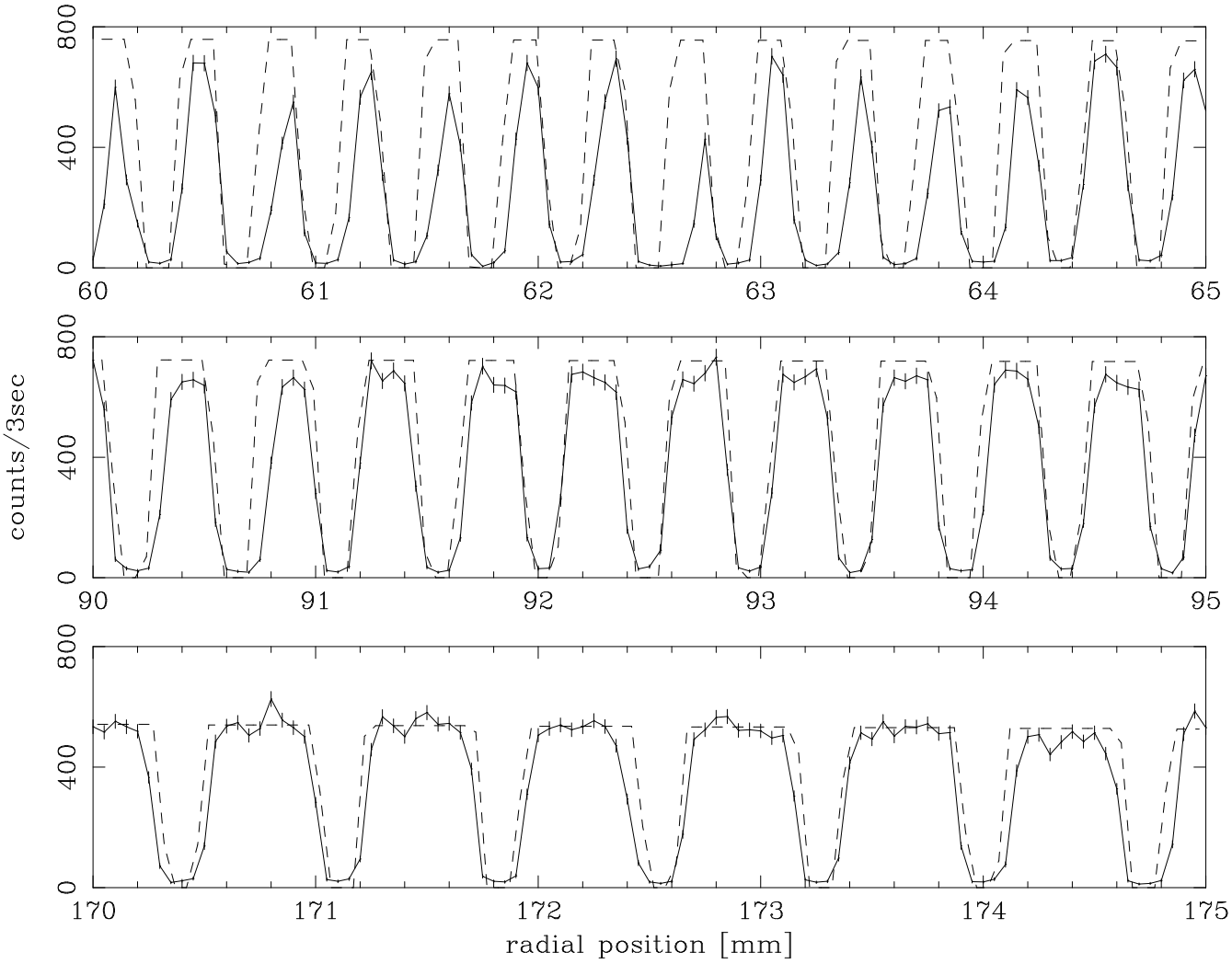

Figure 10, T. Okajima et. al.

Table 1. The list of parameters of each group of supermirror. Each line in the 4th column present parameters of stacked multilayers in order from the reflecting surface toward the substrate.

group	grazing angles [deg.]	N_{total}	(d[nm], N, Γ) (If Γ is not shown, $\Gamma = 0.4$.)
1	0.105–0.125	25	(13.0,1,0.6),(8.0,1),(7.1,3),(6.3,4),(5.8,6),(5.0,10)
2	0.125–0.131	25	(13.0,1,0.6),(8.0,1),(7.1,3),(6.3,4),(5.8,6),(5.0,10)
3	0.131–0.144	25	(13.0,1,0.6),(8.0,1),(7.1,3),(6.3,4),(5.8,6),(5.0,10)
4	0.144–0.158	38	(12.0,1,0.6),(7.1,3),(6.0,5),(5.3,7),(4.9,10),(4.3,12)
5	0.158–0.174	38	(12.0,1,0.6),(7.1,3),(6.0,5),(5.3,7),(4.9,10),(4.3,12)
6	0.174–0.192	41	(10.6,1,0.63),(6.6,2),(5.9,4),(4.9,8),(4.3,11),(3.8,15)
7	0.192–0.210	41	(10.6,1,0.63),(6.6,1),(6.0,4),(5.1,7),(4.5,8),(4.0,9),(3.6,11)
8	0.210–0.232	40	(9.3,1,0.59),(6.3,1),(5.6,3),(5.0,5),(4.5,7),(4.0,10),(3.5,13)
9	0.232–0.256	50	(8.3,1,0.54),(6.3,1),(5.2,5),(4.5,7),(3.9,10),(3.5,12),(3.2,14)
10	0.256–0.281	50	(7.4,1,0.57),(5.4,1),(4.8,3),(4.3,4),(4.0,5),(3.7,8),(3.4,10),(3.1,18)
11	0.281–0.308	63	(5.8,2),(4.5,5),(3.8,8),(3.4,12),(3.1,16),(2.9,20)
12	0.308–0.339	63	(5.8,2),(4.5,5),(3.8,8),(3.4,12),(3.1,16),(2.9,20)
13	0.339–0.356	65	(5.2,3),(4.2,6),(3.7,8),(3.4,10),(3.1,16),(2.9,22)

Table 2. Best fit parameters of reflected X-ray beam profile model

function	parameters	
Gaussian	$N_{gau} = 0.25$	$\sigma_{gau} = 0.65$
Exponential	$N_{exp} = 0.25$	$\sigma_{exp} = 1.11$
Lorentzian	$N_{lo} = 2.85 \times 10^{-3}$	$\sigma_{lo} = 2.50$